ACS APPLIED MATERIALS & INTERFACES

Research Article

Cite This: ACS Appl. Mater. Interfaces 2018, 10, 150−164

www.acsami.org

Porous Au@Pt Nanoparticles: Therapeutic Platform for Tumor Chemo-Photothermal Co-Therapy and Alleviating Doxorubicin-Induced Oxidative Damage

Qian Yang,[§] Jinrong Peng,[†] Yao Xiao,[†] Wenting Li,[‡] Liwei Tan,[#] Xiaohong Xu,[§] and Zhiyong Qian*[,†]

[†]State Key Laboratory of Biotherapy, West China Hospital, and Collaborative Innovation Center of Biotherapy, Sichuan University, No. 17, Section 3, Southern Renmin Road, Chengdu 610041, Sichuan, P. R. China

[§]School of Pharmacy, College Key Laboratory of Sichuan Province for Specific Structure of Small Molecule Drugs, Chengdu Medical College, No. 783, Xindu Avenue, Xindu District, Chengdu 610500, Sichuan, P. R. China

[‡]Department of Pharmacy, West China Second University Hospital, Chengdu 610041, Sichuan, P. R. China

[#]College of Medicine, Southwest Jiaotong University, Chengdu 610031, Sichuan, P. R. China

Supporting Information

ABSTRACT: Nanoparticle-based systems explore not only the delivery efficacy of drugs or contrast agents, but also additional capabilities like reducing the systemic toxicity, especially during cancer chemotherapy. Since some of the noble metal nanoparticles exhibit the catalysis properties which can scavenge the reactive oxygen species (ROS), they can be used as a promising drug delivery platform for reducing the oxidative stress damage in normal tissues caused by some chemotherapy drugs. Herein, in this study, we construct porous Au@Pt nanoparticles and further explore the properties of porous Au@Pt nanoparticles in relieving the oxidative stress damage as well as in tumor growth inhibition by chemo-photothermal co-therapy. The tunable surface pore structure of Au@Pt nanoparticle provides space for Doxorubicin (DOX) loading. cRGD peptide modification enable the DOX-loaded Au@Pt nanoparticles to improve drug delivery properties. The constructed nanocarrier (DOX/Au@Pt-cRGD) shows controlled drug release behavior. Meanwhile, the absorbance peak of the Au@Pt structure in the near-infrared (NIR) portion provides the capacity for *in vivo* photoacoustic imaging and the high photoconversion efficiency, which make Au@Pt nanoparticle a suitable carrier for photothermal therapy (PTT). Combined with chemotherapy, the nanosystem DOX/Au@Pt-cRGD shows enhanced anticancer therapeutic effects. More importantly, ROS-scavenging activity of Au@Pt alleviates the DOX-induced oxidative stress damage, especially the cardiomyopathy during chemotherapy. Herein, this nanosystem DOX/Au@Pt-cRGD could be explored as reactive oxygen scavenger and drug delivery system for side effects relieving chemo-photothermal combinational therapy.

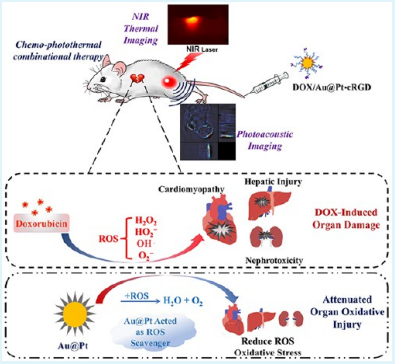

KEYWORDS: *Au@Pt nanoparticles, porous structure, combinational therapy, ROS scavenger, oxidative stress*

INTRODUCTION

During cancer chemotherapy, due to the low selective enrichment of antitumor drug in the tumor region, which results in serious side effects, the therapeutic outcome was not satisfied. As a first-line anticancer drug, Doxorubicin (DOX) has been widely used for the treatment of various cancers. Its applications, however, has been restricted by intolerable adverse effects. It has been confirmed that DOX generated ROS and induced oxidative damage in all major organs.[1] However, cardiotoxicity is one of the serious side effects due to the low level of antioxidant defenses in cardiac tissue compared to other organs, such as liver or kidney.[2] Simultaneous administration of DOX with chemosensitizers (such as Curcumin), antioxidants (Resveratrol), or ROS scavengers (2,2,6,6-tetramethylpiperidine-*N*-oxyl, TEMPO) have been developed and applied to alleviate the oxidative damage during chemotherapy.[3−5] However, the combinational treatment of chemotherapy drugs and chemosensitizers or antioxidants/ROS scavengers faces the drawback of fast elimination *in vivo*. These small molecule agents led to rapid elimination of from the kidney, which might require pretreatment for at least 2 weeks prior to drugs, and most of these combined routes lacked large clinical trials to support their efficacy.[6] Therefore, creative and efficient strategies are highlighted.

Although some nanotechnologies were explored to improve the drug delivery efficiency and control the drug release behavior,[7,8] the adverse effects, especially the damage to vital organs caused by the nontargeted released chemotherapy drugs, still need to be further improved.[9] To address these issues, the tissue-specific and nontoxic nanosystems with

Received: September 27, 2017
Accepted: December 18, 2017
Published: December 18, 2017

DOI: 10.1021/acsami.7b14705
ACS Appl. Mater. Interfaces 2018, 10, 150−164

Scheme 1. Schematic Illustration of Chemo-Photothermal Combinational Therapy for Tumors by the Multifunctional Au@Pt Nanoparticles[a]

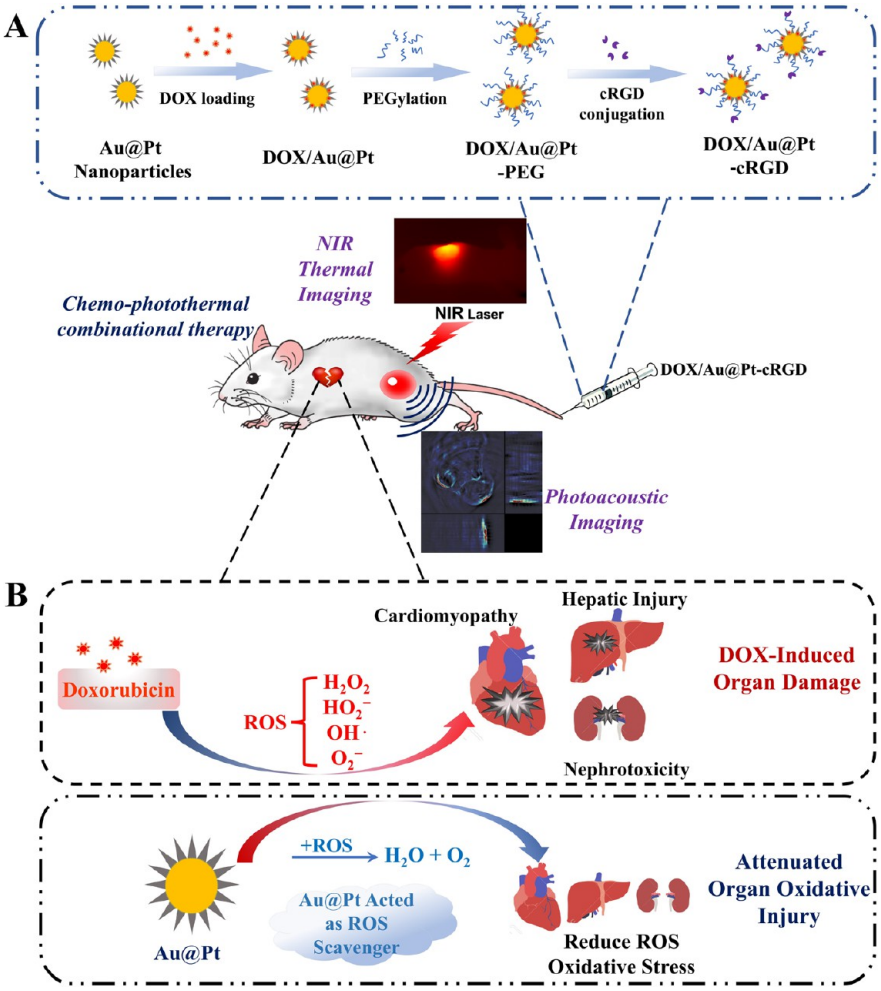

[a](A) Construction of DOX/Au@Pt-cRGD; (B) ROS scavenging property by catalysis of platinum shell endues the nanostructure with attenuating DOX-induced organ oxidative injury, especially the cardiomyopathy during chemotherapy. The gold core-based nanostructure maintains photoacoustic imaging and high photothermal conversion property, while the surface porous platinum shell not only provides the capability for drug loading but also alleviates adverse effects of chemodrugs.

diversity properties provide an alternative choice.[10,11] The redox polymeric nanoparticles with ROS scavenging function have been reported for DOX delivery, increasing the drug enrichment rate at the tumor site while reducing DOX-induced oxidative stress injury.[12,13] In addition, some recent studies have proven that the noble metal nanoparticles such as platinum nanoparticles can reduce the oxidative stress by the SOD/catalase mimetic property, and the stability of metal nanoparticles enhanced their catalysis activity *in vivo*, which would enable promising potential for clinical use in cancer therapy.[14−16]

Generally, gold and platinum are two of the most widely used noble metals in metal based nanoparticle construction. They are biocompatible and have low cytotoxicity for their inertia-driven reactivity *in vivo* and *in vitro*.[17] The types of gold nanoparticles have been designed and fabricated as a multifunctional platform for combinational cancer therapy, especially for chemo-photothermal therapy, since they have outstanding optical properties and photothermal conversion.[18−21] The gold−platinum alloy nanoparticles have generated great interest for their unique catalytic activity, as well as the optical properties. Due to the differences of reduction rates of gold and platinum, the core−shell structure Au@Pt bimetallic nanoparticles with surface nanoporosity would be obtained by modulating the ratio of the noble metal precursors.[22]

Nanocarriers with porous structures have proven their potential and possibilities in drug delivery and nanotheranostics.[23] The porous structures provide a physical 3D space for drug or contrast agent loading, which has attracted enormous attention.[24−26] Because of this structural character, the porous structure of the Pt shell of Au@Pt bimetallic nanoparticles would significantly increase the surface area of Pt, which is expected to maintain better performance in both reducing oxidative stress and drug-loading capability for their specific surface area.[27,28] According to some reports, porous Au@Pt bimetallic nanoparticles with large surface area have been fabricated.[29,30] Furthermore, the Au@Pt nanoparticles exhibited strong absorption in the NIR region, which makes them useful as agents for photothermal therapy (PTT).[31] Based on our previous study, tumor growth cannot be efficiently inhibited by PTT alone.[32] The combination of

DOI: 10.1021/acsami.7b14705
ACS Appl. Mater. Interfaces 2018, 10, 150−164

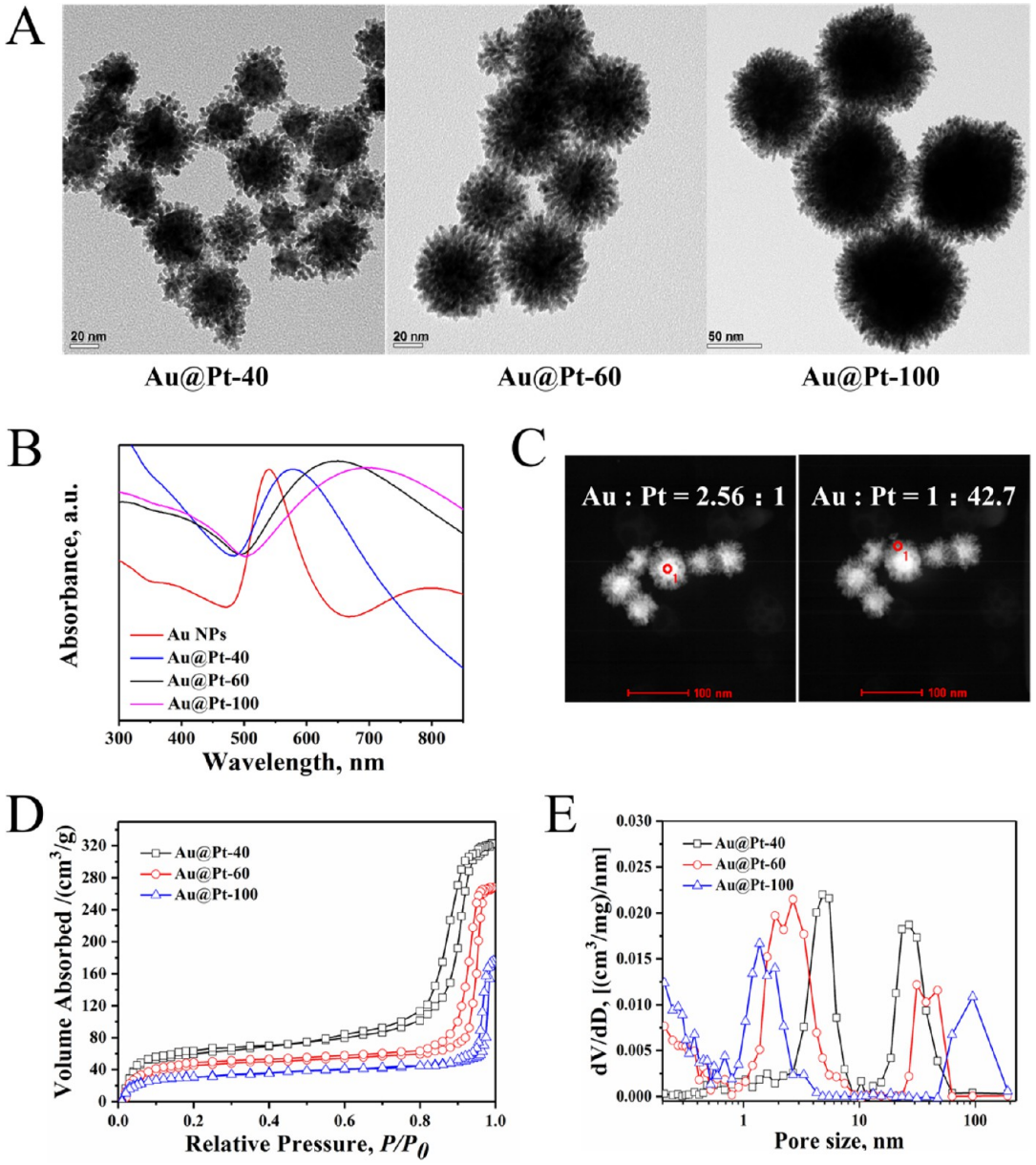

Figure 1. Characterization of porous Au@Pt nanoparticles. (A) TEM images of porous Au@Pt nanoparticles. (B) UV−vis spectra of Au@Pt nanoparticles. (C) STEM image of Au@Pt-60. (D and E) Volume absorbed and pore size distribution of Au@Pt-40, Au@Pt-60, and Au@Pt-100.

PTT and chemotherapy can further inhibit the tumor growth *in vivo*, and even could eliminate the tumor completely.[33−35] However, the porous Au@Pt nanoparticles as a combination therapy platform for chemo-photothermal therapy have not been studied *in vivo* yet; in particular, their ROS scavenging property to reduce oxidative stress caused by chemotherapeutic drugs *in vivo* still needs to be explored further.

So, in this study, we planned to construct porous Au@Pt bimetallic nanoparticles from chloroauric acid (gold precursor) and potassium chloroplatinite (platinum precursor). Based on the different reduction rates of gold precursor and platinum precursor in the ascorbic acid reduction environment, we expected to control the porous structure of the bimetallic nanoparticles by controlling the feeding ratios of gold precursor and platinum precursor, which also controlled the DOX loading capacity of the Au@Pt nanoparticles. Further coating with cRGD by PEG linker after DOX loading increased the colloidal stability and also enabled the nanoparticles' targeting property. We evaluated the drug delivery and photoconversion efficiency of Au@Pt nanoparticles *in vitro* and *in vivo*. Photoacoustic imaging and infrared thermal imaging have been used to investigate the enrichment of Au@Pt nanoparticles in the tumor site. Meanwhile, we also compared the chemo-photothermal therapeutic efficacy with photothermal therapy or chemotherapy in the tumor-bearing mice model. Finally, the simultaneous scavenging of drug-induced ROS by Au@Pt nanoparticles has been validated on a DOX-induced organ injury model (Scheme 1). The results demonstrated that the porous Au@Pt nanoparticles are promising candidates for photoacoustic imaging guided DOX delivery and a chemo-photothermal combination therapy platform with oxidative stress reduction.

RESULTS AND DISCUSSION

Preparation and Characterization Porous Au@Pt Nanoparticles. The porous Au@Pt nanoparticles were

DOI: 10.1021/acsami.7b14705
ACS Appl. Mater. Interfaces 2018, 10, 150−164

Table 1. Compositional Ratios of the Porous Au@Pt Nanoparticles Synthesized

sample code	H_2PtCl_4 (20 mM)	$HAuCl_4$ (20 mM)	Pluronic F127	AA solution (200 mM)	Pt/Au molar ratio	particle size (By TEM)	particle size (By DLS)	PDI
Au@Pt-40	1 mL	2 mL	30 mg	1.5 mL	0.5	39.5 ± 4.2	48.6 ± 2.2	0.22
Au@Pt-60	2 mL	2 mL	40 mg	2 mL	1	56.8 ± 5.4	67.4 ± 3.6	0.29
Au@Pt-100	4 mL	2 mL	60 mg	3 mL	2	101.6 ± 7.9	115.3 ± 4.8	0.27
[a]	6 mL	2 mL	80 mg	4 mL	3	-	995 ± 86.7	0.92

[a]When the Pt/Au molar ratio reached 3, no stable porous Au@Pt nanoparticles could be obtained.

synthesized by modified ultrasonochemical procedure which deposited the highly branched platinum shell on the gold core with simultaneous coreduction by ascorbic acid, according to the previous report.[29] By optimizing the synthesis parameters, especially with four calculated molar ratios of Pt/Au, Au@Pt nanoparticles with size distributions ranging from ∼40 to ∼100 nm (ImageJ software was used to calculated about 100 numbers of nanoparticles from the TEM images for each sample) were obtained, which were named Au@Pt-40, Au@Pt-60, and Au@Pt-100 (Figure 1A). The hydrodynamic diameter of different Au@Pt samples was also studied by dynamic laser scattering (DLS) and correlated with the size distributions by TEM (Table 1). The proportion of Au and Pt contents of each sample was measured by inductively coupled plasma-atomic emission spectrometer (ICP-MS), and the results were listed in Table S1. The layer thicknesses of the Pt shell observed by TEM were increased from about 8 nm (Au@Pt-40) to 15 nm (Au@Pt-60) by adding more Pt solution. When the Pt/Au molar ratios were further increased to 2 (Au@Pt-100), the thickness of the Pt shell changed little but the particle size increased to more than 100 nm (Figure 1A). Moreover, with the Pt shell deposited on the bare Au surface, the plasmon absorption peak of gold showed an obvious red shift with a decrease of the SPR intensity, compared to that of gold nanoparticles (Figure 1B). The core−shell structure of nanoparticles was further demonstrated by the high-resolution transmission electron microscope (HR-TEM) and scanning transmission electron microscopy (STEM).[30] As shown in Figure S1A, the observed *d*-spacings (0.22 nm) in the lattice fringes regions correspond to the {111} planes of the Pt branch structure. Moreover, the elemental distribution of Pt and Au on a single particle was further clarified by STEM and energy-dispersive X-ray (EDX) spectroscopy (Figures 1C and S1C). The compositional ratios of Au and Pt in the core and at the edge of the Au@Pt nanoparticles were measured with proportions of 2.56:1 and 1:42.7, respectively. The cross-sectional compositional line profile showed that the Pt content decreased, while the Au content was increased accordingly from the edge to the inner core of the Au@Pt nanoparticles, indicating the Au core and Pt shell structure (Figure S1B).

The structure of Au@Pt was further identified by X-ray photoelectron spectroscopy (XPS), as shown in Figure S1D. XPS analysis of Au@Pt nanocparticles showed significant Pt 4f peaks (Pt $4f_{7/2}$ at 71.5 eV and Pt $4f_{5/2}$ at 74.8 eV) corresponding to the binding energy of the Pt metal. The binding energy of metallic Au in Au@Pt nanoparticles (Au $4f_{5/2}$ at 87.9 eV and Au $4f_{7/2}$ at 83.6 eV) was detected as being much weaker than that in Au nanoparticles, which would contribute to the surface composition of Pt shell partly shielding the core, indicating the formation of a core−shell structure.[36]

By nitrogen adsorption−desorption measurements, we further identified the nanoporous structure of the Au@Pt nanoparticles. The pore volumes of Au@Pt-40, Au@Pt-60, and Au@Pt-100 were 321.8, 267.8, and 174.6 cm^3/g, respectively (Figure 1D). This indicated that the pore volumes decreased as the Pt/Au feeding ratios increased. By calculation, we obtained the pore sizes of Au@Pt-40, Au@Pt-60, and Au@Pt-100 as 4.8, 2.7, and 1.3 nm, respectively (Figure 1E). In combination with the TEM results, we can conclude that the Pt shell is overgrown in Au@Pt-100 while it is undergrown in Au@Pt-40. In order to attain optimized drug loading capacity, we want to maintain a suitable nanoporous structure of Au@Pt with adapted small pore size. Therefore, we chose Au@Pt-60 for further applications.

Construction of DOX/Au@Pt-cRGD. DOX was chosen as a model anticancer drug. It exhibits good interaction with metal surface and is expected to be absorbed in the pore structure of Au@Pt nanoparticles. Purified Au@Pt solution were incubated with DOX at pH 8 for drug loading, since DOX could be deprotonated at basic pH.[37] From the TEM imaging (Figure 2A), the particle size and appearance of DOX/Au@Pt did not show any morphologic change, compared with the bare Au@Pt nanoparticles. To optimize the ratio of DOX and Au@Pt, the loading capability and yield were calculated by quantifying the unabsorbed DOX in the supernatant (Table 2). The results showed that the highest DOX loading content could reach 10.2% (w/w) and the yield was about 52.3%, when the DOX/Au@Pt ratio was 1:4 (w/w). However, it was easily aggregated, which may reduce the enrichment of the nanoparticles in the tumor site. Further coating with PEG avoids particle aggregation by increasing the colloidal stability.[38] In addition, bifunctionalized PEG linker also enabled the nanocarrier's active targeting property by cRGD peptide conjugation. After functionalization with PEG linker and cRGD, a layer of polymer coating could be observed on the surface of Au@Pt nanoparticles in the TEM image (Figure 2A). In the following study, the DOX loading capability of DOX/Au@Pt-cRGD was settled as 4.8% (w/w) (Table 2). In addition, the average sizes of DOX/Au@Pt-PEG and DOX/Au@Pt-cRGD were about 78.4 and 85.3 nm with PDIs of 0.178 and 0.196, respectively, by DLS measurement, which slightly increased in comparison to Au@Pt (Figure 2B), and the surface charges were about −0.8 mV and −14.8 mV, respectively, which was opposite that of DOX/Au@Pt (+11.4 mV) (Figure 2C). According to DLS real-time measurement, DOX/Au@Pt-cRGD maintained its size distribution after being dispersed in different mediums (water, phosphate buffered saline (PBS, pH = 7.4), serum, and DMEM medium with 10%FBS) in 24 h (Figure 2D). Even after 72 h of storage in water or DMEM medium, slight increases in hydrodynamic diameter and PDI were observed, compared with the freshly prepared nanoparticles (85.3 ± 4.8 nm, with PDI of 0.196), which indicated its stability in a biorelevant environment (Figure S2A).

DOI: 10.1021/acsami.7b14705
ACS Appl. Mater. Interfaces 2018, 10, 150−164

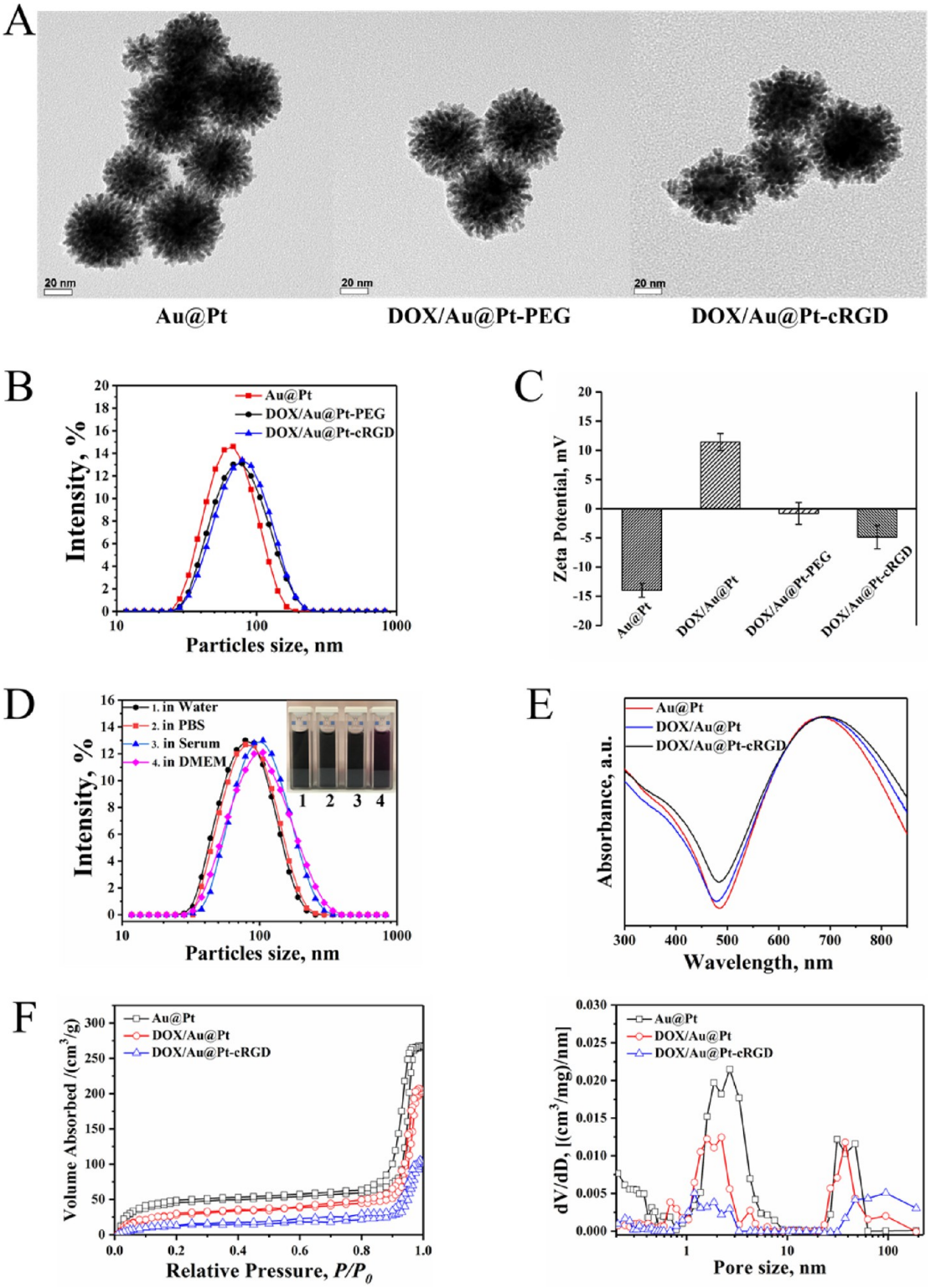

Figure 2. (A) TEM imaging of Au@Pt, DOX/Au@Pt-PEG, and DOX/Au@Pt-cRGD, respectively. (B and C) Size distribution of corresponding samples. (D) Particle size distribution of DOX/Au@Pt-cRGD in different mediums. (E) UV−vis spectra of corresponding samples. (F) Volume absorbed and pore size distribution of corresponding samples.

Furthermore, with DOX loading and PEG-cRGD conjugation, the surface pore sizes and N_2 absorption capacities of DOX/Au@Pt and DOX/Au@Pt-cRGD were dramatically decreased, which could be attributed to the space occupied by DOX and PEG molecules (Figure 2F). Additionally, the surface modification of Au@Pt nanoparticles was monitored by UV−vis absorption spectra, and no obvious peak shifts were revealed in the UV−vis spectra for both DOX/Au@Pt and DOX/Au@Pt-cRGD, compared with Au@Pt (Figure 2E).

Photothermal Conversion Drug Release Profile of DOX/Au@Pt-cRGD. After functionalization, the DOX/Au@Pt-cRGD aqueous solution still had strong absorption in the

DOI: 10.1021/acsami.7b14705
ACS Appl. Mater. Interfaces 2018, 10, 150−164

Table 2. Properties of Different Au@Pt Conjugates after DOX Loading

sample code	DOX/Au@Pt ratio (w/w%)	drug loading capacity (%)	yield (%)	particle size (by DLS)	PDI
DOX/Au@Pt 1	1:9	4.97	49.7	787.8 ± 25.6[a]	0.85
DOX/Au@Pt 2	1:4	10.21	51.05	753.4 ± 24.7[a]	0.66
DOX/Au@Pt 3	1:3	9.89	39.56	894 ± 45.6[a]	0.89
DOX/Au@Pt-PEG	1:9	4.78	47.8	78.4 ± 3.6	0.178
DOX/Au@Pt-cRGD	1:9	4.82	48.2	85.3 ± 4.8	0.196

[a]DOX/Au@Pt nanoparticles were unstable and aggregated easily before PEGylation and conjugation.

near-infrared region near 700 nm, which indicated the potential as a nanocarrier for photothermal therapy. The photothermal conversion was investigated by monitoring the temperature increase while exposing it to 808 nm laser (1.5 W/cm^2) for different periods. As depicted in Figure 3A, the final temperatures of DOX/Au@Pt-cRGD solution with Au@Pt concentrations from 0 to 100 μg/mL were increased from 27.3 to 68.9 °C after irradiation for 5 min which demonstrates that DOX/Au@Pt-cRGD can significantly generate heat with excitation from NIR light. In comparison, no significant temperature change was observed when saline was exposed to the same NIR laser. It is more obvious from the infrared thermal images taken from the nanoparticle dispersion (50 μg/mL of Au@Pt) at 1, 3, and 5 min under NIR laser irradiation (Figure 3A, right inset). After eight on−off irradiation cycles, the morphology of DOX/Au@Pt-cRGD showed no affect, and the dispersion still maintained its high photothermal conversion efficacy with similar absorption in the NIR region (Figures 3B, S2B, S2C). As some research reported, most of the cancer cells are susceptible to hyperthermia, especially when increasing the environment temperature to more than 43 °C can trigger apoptosis and necrosis.[39] Therefore, DOX/Au@Pt-cRGD can be selected as a potential candidate for cancer photothermal therapy.

We then evaluated the release behavior of DOX/Au@Pt-cRGD. When the pH values approach the environment of the tumor site and cytoplasm (pH 6.0 and 5.0), the accumulated release of DOX was almost 60% and 80% in 48 h, respectively (Figure 3C). In contrast, only 30% of the drug was released from DOX/Au@Pt-cRGD in the physiologic conditions (pH = 7.4). It indicated that the DOX release from the nanocarrier was pH responsive. pH-dependent drug release property from Au@Pt platform is mainly ascribed to the accelerated dissociation of DOX in acidic environment.[40] Furthermore, the increase of temperature may also enhance the solubility and diffusion of drugs. Due to the high photothermal conversion efficacy, DOX released from DOX/Au@Pt-cRGD can also be accelerated by NIR irradiation. Within 5 min of NIR laser irradiation (1.5 W/cm^2), the accumulated drug release was faster than that without laser irradiation. Almost 80% of DOX was released in the initial 12 h after several on−off cycles of laser irradiation in medium at pH 6, and more than 96% drug release was achieved in the same incubation time at pH 5 environment with similar laser irradiation (Figure 3D). The enhanced DOX release triggered by NIR laser would

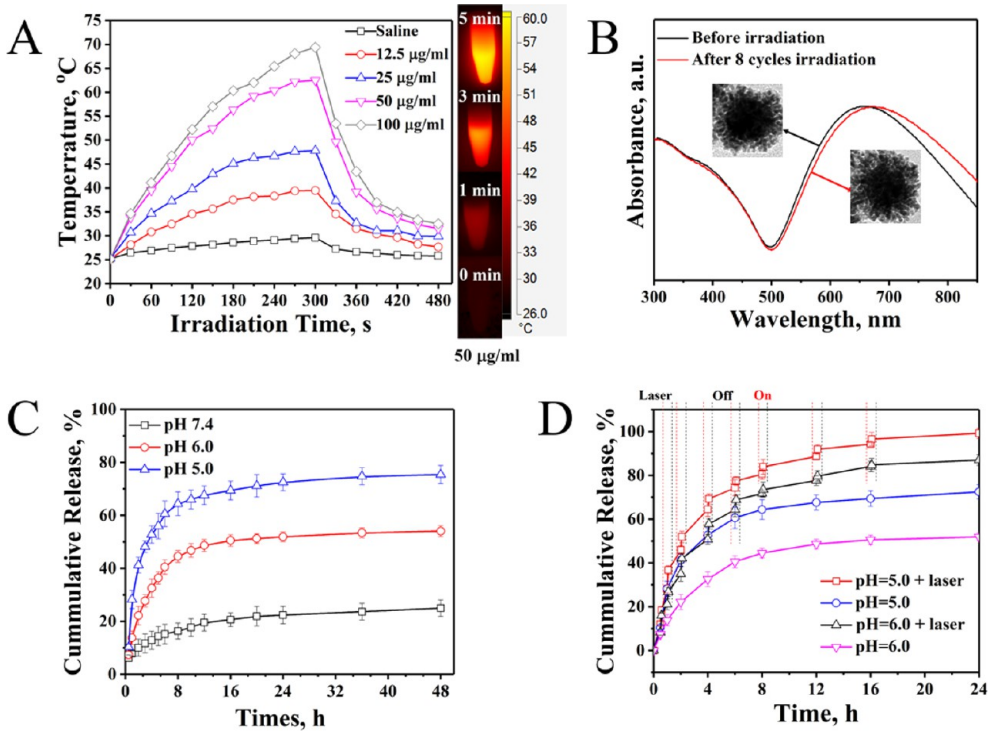

Figure 3. (A) Photothermal conversion of DOX/Au@Pt-cRGD with different concentrations under 808 nm laser irradiation (laser power: 1.5 W/cm^2). (B) Stability of DOX/Au@Pt-cRGD after eight cycles of laser irradiation (laser power: 1.5 W/cm^2). (C and D) DOX release profiles of DOX/Au@Pt-cRGD in different pH environments (with or without laser irradiation).

DOI: 10.1021/acsami.7b14705
ACS Appl. Mater. Interfaces 2018, 10, 150−164

be attributed to increased solubility in response to additional heat of the surrounding environment mediated by the photothermal effect of Au@Pt. Therefore, the drug release from DOX/Au@Pt-cRGD is pH/NIR dual triggered.

Tumor Cell Growth Inhibition by DOX/Au@Pt-cRGD Mediated PTT *In Vitro*. Before its application to cancer cells, the cellular uptake was performed by incubating MDA-MB-231cell with DOX/Au@Pt-PEG and DOX/Au@Pt-cRGD. Owing to the SPR of Au@Pt, it was hard to label it with fluorescent dye to evaluate the cellular uptake. Hence, ICP-MS was used to detect the intracellular contents of elemental Au and Pt. The results indicated that the uptake of Au@Pt conjugates depended on incubation time, and the cRGD conjugated nanosystems could enable higher enrichment in MDA-MB-231 cells in the first 4 h (Figure S3).

To investigate whether thermotherapy and chemotherapy showed coinhibition effect or not, the MDA-MB-231 cell growth inhibition mediated by Au@Pt-cRGD, DOX/Au@Pt-PEG, and DOX/Au@Pt-cRGD at different concentrations with or without NIR laser irradiation were quantified by MTT assay (Figure 4A). The cell survival was over 90% even after incubation with Au@Pt-cRGD at the mean concentration of 333 μg/mL, indicating the low toxicity of the nanocarriers at the cellular level. The half-maximal inhibitory concentration (IC_{50}) of DOX/Au@Pt-cRGD without any laser irritation was 4.02 μg/mL (as concentration of DOX), a little higher than that of the free DOX (3.45 μg/mL), which might be due to the intracellular incomplete DOX release. Au@Pt-cRGD with NIR laser treatment (808 nm, 1.5 W/cm^2, 5 min) showed photothermal therapeutic effects with an IC_{50} concentration of 37.5 μg/mL. More importantly, DOX/Au@Pt-cRGD and DOX/Au@Pt-PEG groups upon NIR irradiation with the IC_{50} of 0.92 and 1.01 μg/mL (as concentration of DOX), respectively, displayed much more efficient tumor cell growth inhibition than that without laser irradiation did, indicating that combination therapy exhibited a coeffect for inhibiting tumor cell growth *in vitro*, while the slightly higher uptake of DOX/Au@Pt-cRGD compared to that of DOX/Au@Pt-PEG may be another reason for the better photothermal efficiency of cRGD conjugated nanosystems.

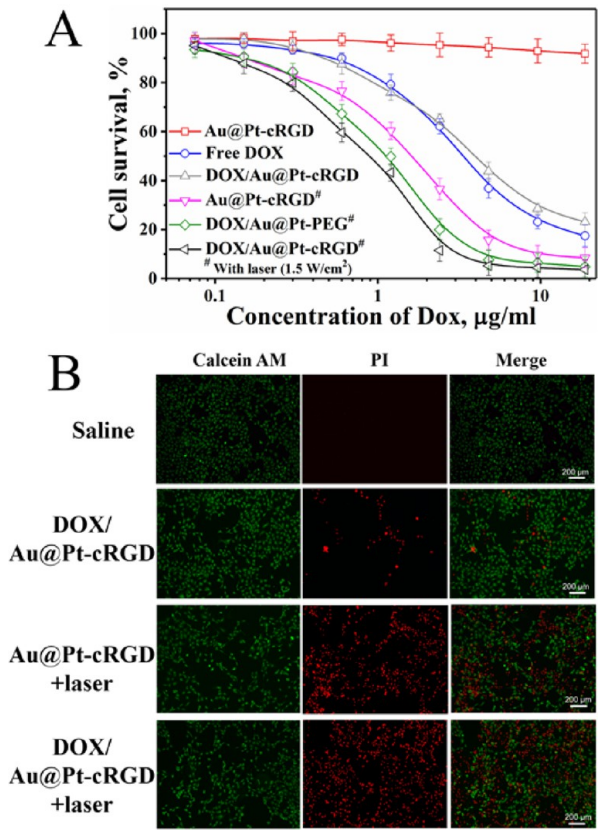

Figure 4. (A) Living cell survival with different treatments on MDA-MB-231 cells for 24 h was determined by MTT assay (concentration of nanocarrier was according to the drug loading capability). Data displayed as mean ± SD (n = 6). (B) Calcein/PI costaining of MDA-MB-231 cells after photothermal ablation mediated by DOX/Au@Pt-cRGD, Au@Pt-cRGD with laser, and DOX/Au@Pt-cRGD with laser (25 μg/mL). Scale bar = 200 μm.

Meanwhile, Calcein AM/PI costaining was adopted to assess the combined therapeutic effect of each group on MDA-MB-231 cells. The results displayed in Figure 4B showed that after 4 h incubation of the samples in the dark, the culturing medium was replaced by fresh culture medium before the introduction of laser irradiation. A few dead cells were observed in the DOX/Au@Pt-cRGD without the laser treated group, which revealed that thermotherapy only could not achieve the desired inhibition effect. In contrast, the groups treated with DOX/Au@Pt-cRGD plus laser irradiation exhibited dramatically decreased survival of living cells even at a low concentration of 25 μg/mL, which also exhibits better cell growth inhibition than Au@Pt-cRGD plus laser irradiation did, which indicated that the DOX/Au@Pt-cRGD is a suitable nanosystem for photothermal therapy/chemotherapy co-therapy for breast cancer.

Enrichment of DOX/Au@Pt-cRGD in Tumor Site *In Vivo*. Since the absorbance peak of Au@Pt appeared at about 680 nm in UV−vis spectra, we tested the photoacoustic (PA) signal of Au@Pt *in vitro*, and the result showed that the PA signal intensity linearly increased with the concentration of Au@Pt (Figure S4), which indicated that Au@Pt based nanomaterials possessed the capacity for *in vivo* fast multi-spectral optoacoustic tomography (MSOT) imaging as the contrast agent. Further, the MSOT approach was performed for tumor diagnosis and the accumulation behavior of the nanomaterials. After being intravenously administered with DOX/Au@Pt-PEG and DOX/Au@Pt-cRGD (both at a concentration of 10 mg/kg) to two groups of subcutaneous MDA-MB-231 tumor bearing Balb/C nude mice, respectively, PA imaging and PA signal intensity of inside the tumor were recorded at different time points (preinjection, and 2, 8, 24, and 48 h after tail-vein injection, Figure 5A). The PA signal of the tumor site was significantly enhanced dramatically from 2 to 8 h, especially in the cRGD conjugated group, which indicated that more DOX/Au@Pt-cRGD was enriched in the tumor site than DOX/Au@Pt-PEG did. The comparison of PA signal in the tumor site was further supported by the MSOT intensity (Figure 5B). No significant difference of the PA signal intensity could be observed between that DOX/Au@Pt-cRGD and DOX/Au@Pt-PEG treated groups in the initial 4 h. After 24 h, the PA signal intensity of the tumor site treated with DOX/Au@Pt-cRGD was 1.4-fold higher than that of the DOX/Au@Pt-PEG group.

We further quantified the enrichment of Au@Pt nanoparticles in tumor regions by measuring the total Au and Pt contents in tissues via ICP-MS (Figure 5C). The Au@Pt nanoparticles are mainly distributed in the liver, kidney, tumor, and lung, 4 h after the injection of nanoparticles, and no

DOI: 10.1021/acsami.7b14705
ACS Appl. Mater. Interfaces 2018, 10, 150−164

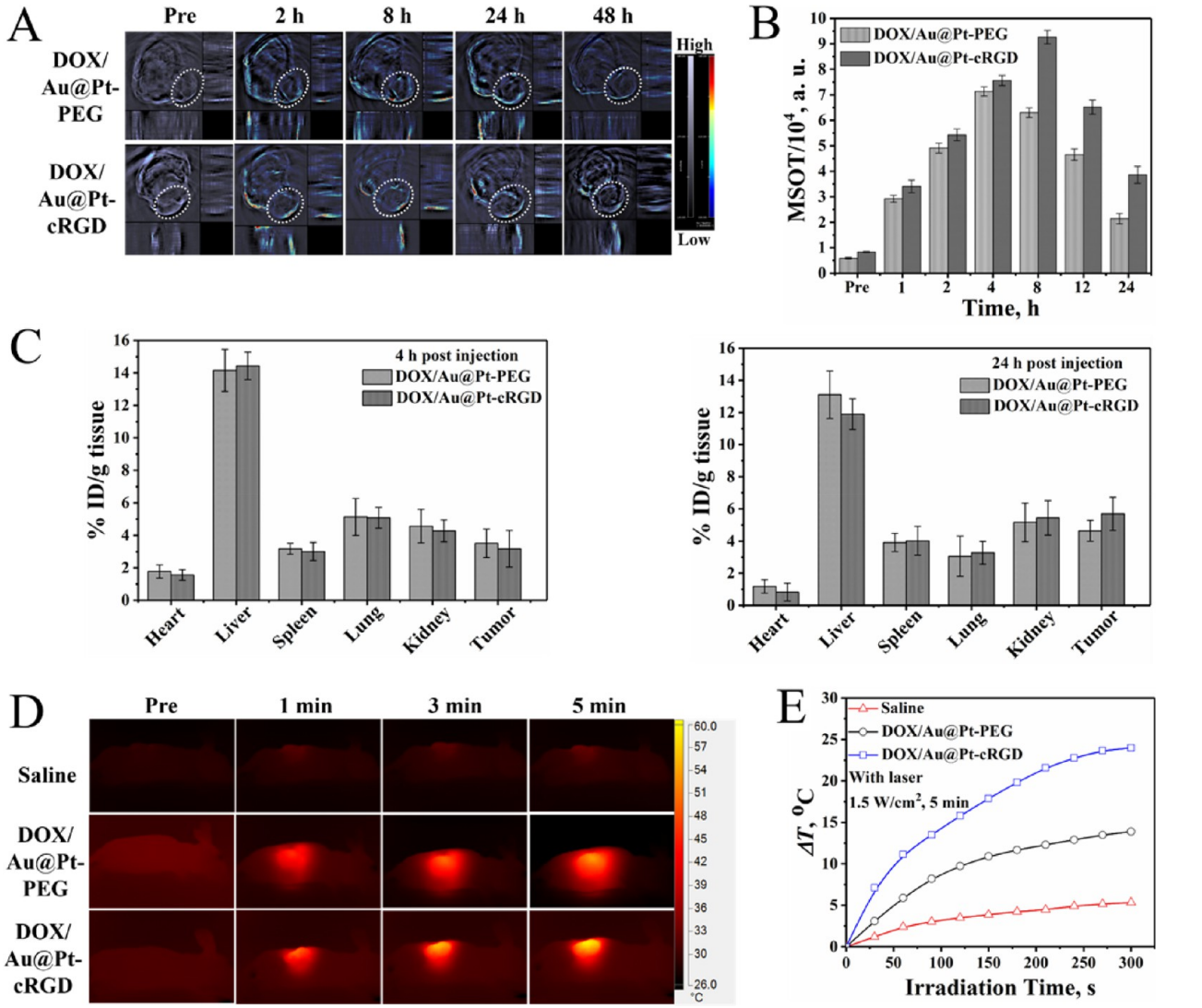

Figure 5. Au@Pt-mediated imaging-guided *in vivo*. (A) PA imaging of MDA-MB-231 tumor-bearing mice *in vivo* before and after the intravenous administration of DOX/Au@Pt-PEG and DOX/Au@Pt-cRGD. (B) MSOT intensity variation of the tumor tissue vs time *in vivo*. (C) Biodistribution of Dox/Au@Pt-cRGD in the main organs and tumors at 4 and 24 h after injection determined by ICP-MS measurement (the total concentrations of Au and Pt). (D) Photothermal conversion of DOX/Au@Pt-cRGD *in vivo*. (E) Relationships of the DOX/Au@Pt-cRGD dose and the photothermal conversion efficiency *in vivo*. Error bars were based on standard deviations (SD) of three mice per group.

remarkable difference was observed between DOX/Au@Pt-cRGD treated group and DOX/Au@Pt-PEG treated group. As time went on, more Au and Pt were detected in tumor tissue of the DOX/Au@Pt-cRGD treated group, compared with the DOX/Au@Pt-PEG treated group after 24 h. The results also demonstrated the enhancement of the enrichment of Au@Pt nanoparticles with the modification of cRGD.

We then used Infrared Thermal Imaging to further evaluate the accumulation of DOX/Au@Pt-cRGD in tumor xenograft. Au@Pt nanoparticles are proven to be a promising candidate for photothermal therapy after intravenous injection of DOX/Au@Pt-PEG and DOX/Au@Pt-cRGD to different mice groups. In 24 h, NIR laser irradiation was introduced. The surface temperatures of the tumor site were recorded (Figure 5D and E). The tumor surface temperatures of the DOX/Au@Pt-cRGD treated group were increased to 60 °C in 5 min of irradiation, which is much faster than the DOX/Au@Pt-PEG treated groups (51 °C in 5 min). The results further demonstrated the enhanced enrichment of Au@Pt nanoparticles in the tumor region after modification of cRGD.

Based on the result of the tumor region enrichment experiment *in vivo*, the DOX/Au@Pt-cRGD showed better selective delivery efficiency than that of DOX/Au@Pt-PEG did, so we chose DOX/Au@Pt-cRGD as an ideal drug delivery platform in the further tumor growth inhibition study.

Tumor Growth Inhibition of DOX/Au@Pt-cRGD Mediated PTT/Chemotherapy *In Vivo*. We have evaluated the tumor growth cell inhibition of DOX/Au@Pt-cRGD *in vitro*, and the results indicated that DOX/Au@Pt-cRGD has potential in PTT/chemotherapy co-therapy of breast cancer cells. Herein, we further investigated the tumor growth inhibition of DOX/Au@Pt-cRGD *in vivo*. Although Au@Pt nanoparticles have been investigated for photothermal therapy at the cellular level in some other reports,[31] limited work has been done for the application of thesee bimetallic nanoparticles, especially the use for chemo-photothermal co-therapy. MDA-MB-231 tumor xenograft models were estab-

DOI: 10.1021/acsami.7b14705
ACS Appl. Mater. Interfaces 2018, 10, 150−164

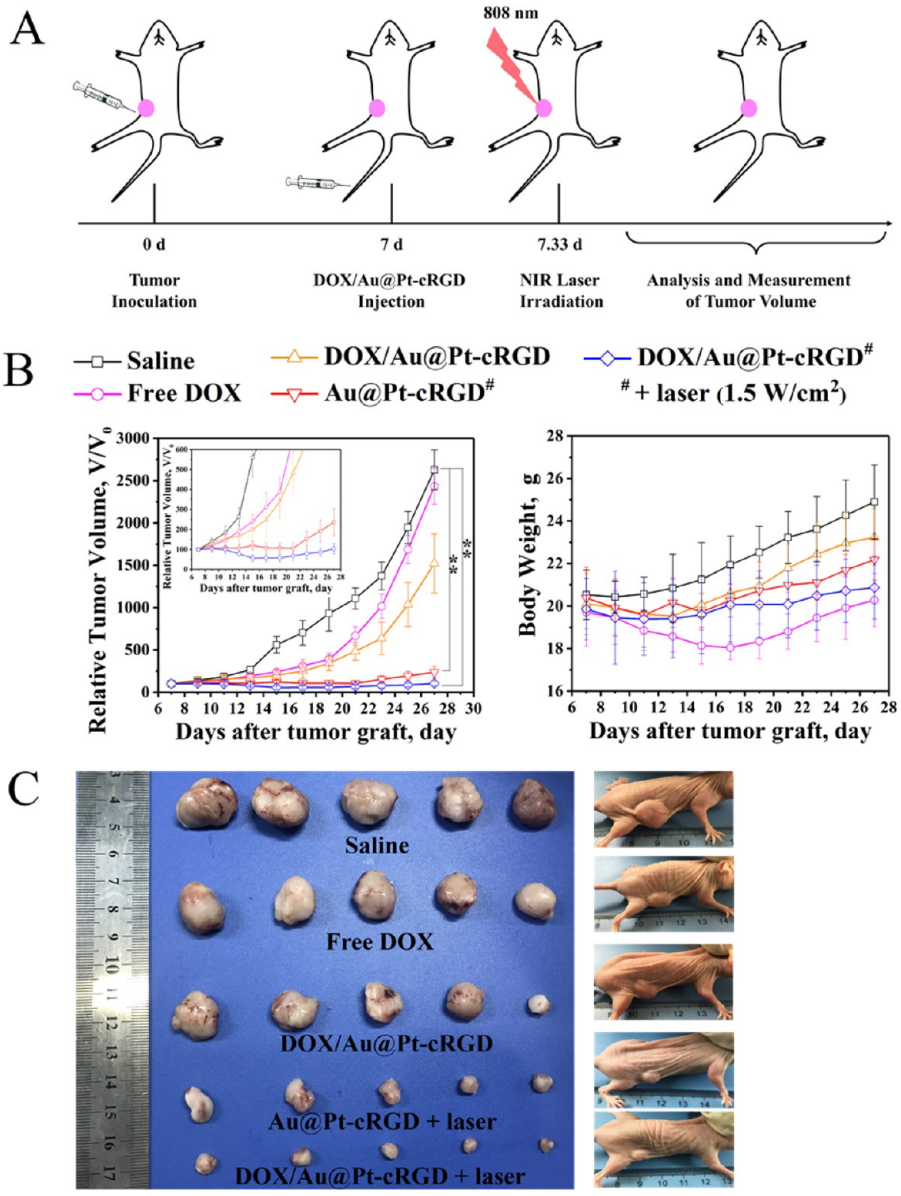

Figure 6. Comparison of the therapeutic efficacy of free DOX, DOX/Au@Pt-cRGD, Au@Pt-cRGD + laser, and DOX/Au@Pt-cRGD + laser in MDA-MB-231 tumor-bearing mice. (A) Schematic illustration of DOX/Au@Pt-cRGD based PTT and chemotherapy to inhibit tumor growth. (B) Relative tumor volume and body weight variation of the mice in different groups during treatment. (C) Photographs of subcutaneous tumors and the tumor-bearing mice taken 3 weeks after different treatments. Error bars were based on standard deviations (SD) of five mice per group (** $P < 0.01$).

lished in Balb/c nude mice. While the tumor size grew to ~100 mm^3, the mice were double-blind randomly divided to five groups, then treated with saline, free DOX, DOX/Au@Pt-cRGD, Au@Pt-cRGD+Laser, and DOX/Au@Pt-cRGD+Laser, respectively (Figure 6A). Further, the tumor volume and body weight of the mice were recorded at a one-day interval. The tumors treated with DOX/Au@Pt-cRGD grew more slowly than that of the free DOX treated group (Figure 6B and D), which indicated that DOX/Au@Pt-cRGD can efficiently deliver DOX to the tumor site. However, by chemotherapy alone, satisfactory tumor growth inhibition cannot be achieved; the tumors grew rapidly after 21 days. Compared to the control group (saline) and chemotherapy group (DOX/Au@Pt-cRGD), the tumor growth was significantly inhibited in the chemo-photothermal combined treatment group (DOX/Au@Pt-cRGD+Laser), which indicated that the chemotherapeutic effects have been enhanced by PTT. Tumors in the PTT treatment group (Au@Pt-cRGD+Laser) showed better inhibition performance than that of the chemotherapy group; however, recurrence happened in some treated mice due to the incomplete ablation, as shown in Figure 6D. In addition, the body weight of mice showed no significant changes among the DOX/Au@Pt-cRGD, Au@Pt-cRGD+Laser, and DOX/Au@Pt-PEG + Laser treated groups, whereas after 4 times of free DOX treatment, a rapid reduction of the body weight of mice was observed, indicating systemic toxicity of DOX (Figure 6C). The anticancer performance of DOX/Au@Pt-cRGD is further proven by the immunohistochemical/immunofluorescence analysis of the tumor tissues with different treatments (Figures 7, S5). Apoptosis and necrosis were observed in the DOX/Au@Pt-cRGD + Laser treated group, while tumor cell proliferation was also inhibited.

DOI: 10.1021/acsami.7b14705
ACS Appl. Mater. Interfaces 2018, 10, 150−164

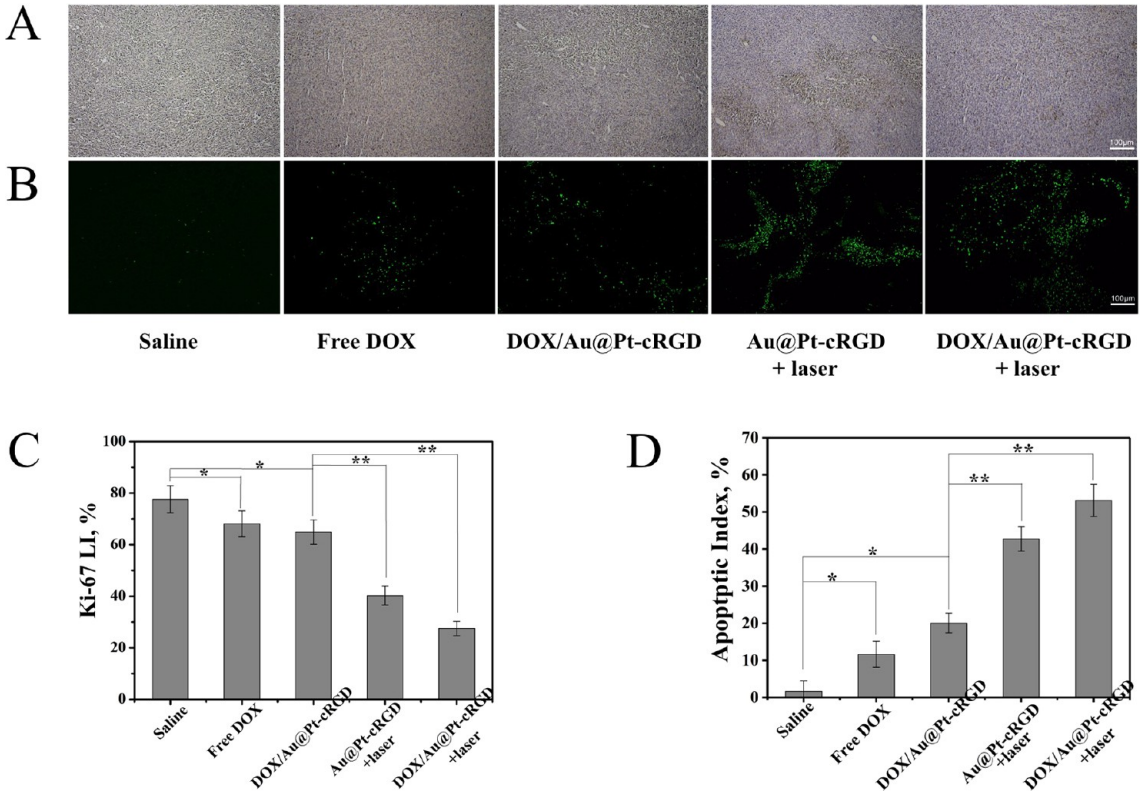

Figure 7. Representative K_i-67 and TUNEL staining for different treatments in MDA-MB-231 model (Scale bar = 100 μm). (A) K_i-67 immunohistochemical and (B) TUNEL immunoflourescent staining in each group; (C and D) are the quantitative analysis of K_i-67 and TUNEL in each group, respectively. Statistical difference between groups (* $P < 0.05$, ** $P < 0.01$).

Alleviation of DOX-Induced Oxidative Stress in Major Organs by Au@Pt Nanoparticles. Dox-induced oxidative damage has been known in all major organs, and can especially cause significant injury to cardiomyocytes, through over-production of ROS.[41] In recent studies, Pt-coated AuNRs (PtAuNRs) maintained PTT efficacy for inducing cell death as AuNRs; in addition, it also showed an effective ROS scavenging effect generated in the inflammation accumulation sites during PPT treatment.[42] If Au@Pt nanoparticles also show an ROS scavenging effect to suppress the oxidative stress of DOX-induced cardiomyopathy, they would be an ideal nanocarrier for DOX delivery. H&E staining was performed to evaluate main organ tissue toxicity. Moreover, to confirm the reduction of the oxidative stress property of Au@Pt nanoparticles, levels of ROS under oxidative stress conditions were determined by DHE staining and carbonylated protein detection.[43,44]

As described, blood was collected, and tissue samples including heart, liver, and kidney were harvested at the end of the experiment (day 10). The increase of alanine aminotransferase (ALT) and aspartate aminotransferase (AST) indicates liver injury in the free DOX treated group. Both Au@Pt-cRGD after DOX injection and DOX/Au@Pt-cRGD treated groups showed no obvious adverse influence, which suggested that Au@Pt treatments at the administered dose were safe and would partly reverse the DOX-induced toxicity. No statistically significant difference was observed of the plasma creatinine (CRE) and urea nitrogen (BUN) that represent kidney function in control and the treated groups (Figure S6A).

Histopathology data indicated that the free DOX treated group displayed the most morbidity damage in cardiac tissues, and slight pathological changes and necrosis could be observed in liver and kidney tissue sections. In contrast, Au@Pt-cRGD administration after or combined with DOX treatment exhibited reduced organ toxicity compared to free DOX (Figure S6B).

DHE staining was used to determine the production of DOX-induced ROS. When oxidized by superoxide anions, DHE would show red-fluorescence in the cytosol.[45] In a free DOX treated control group, the intensity of DHE fluorescence was significantly elevated, suggesting an overproduction of ROS. However, administration of Au@Pt-cRGD after DOX injection significantly decreased the DHE fluorescence intensity, demonstrating an inhibitory effect on oxidative stress. Furthermore, the DOX/Au@Pt-cRGD treated group showed the lowest level of DHE fluorescence, indicating an optimized antioxidative effect (Figure 8A and B).

Protein carbonylation in heart, liver, and kidney tissues provides information about DOX-induced oxidative stress which directly related to cardiac and hepatic toxicity.[46] Carbonyl groups were detected via derivatization with 2,4-dinitrophenyl (DNP) hydrazine. The highest amount of carbonylated proteins were observed after the high dose of free DOX administration, in total cardiac, hepatic, and nephritic protein, which indicated the most serious oxidative stress damage. The Au@Pt as well as DOX treatment (administrated subsequently or simultaneously) significantly decreased the carbonyl amount, compared to the free DOX treated control group. Treatment with DOX/Au@Pt-cRGD in combination resulted in a somewhat lower amount of

DOI: 10.1021/acsami.7b14705
ACS Appl. Mater. Interfaces 2018, 10, 150−164

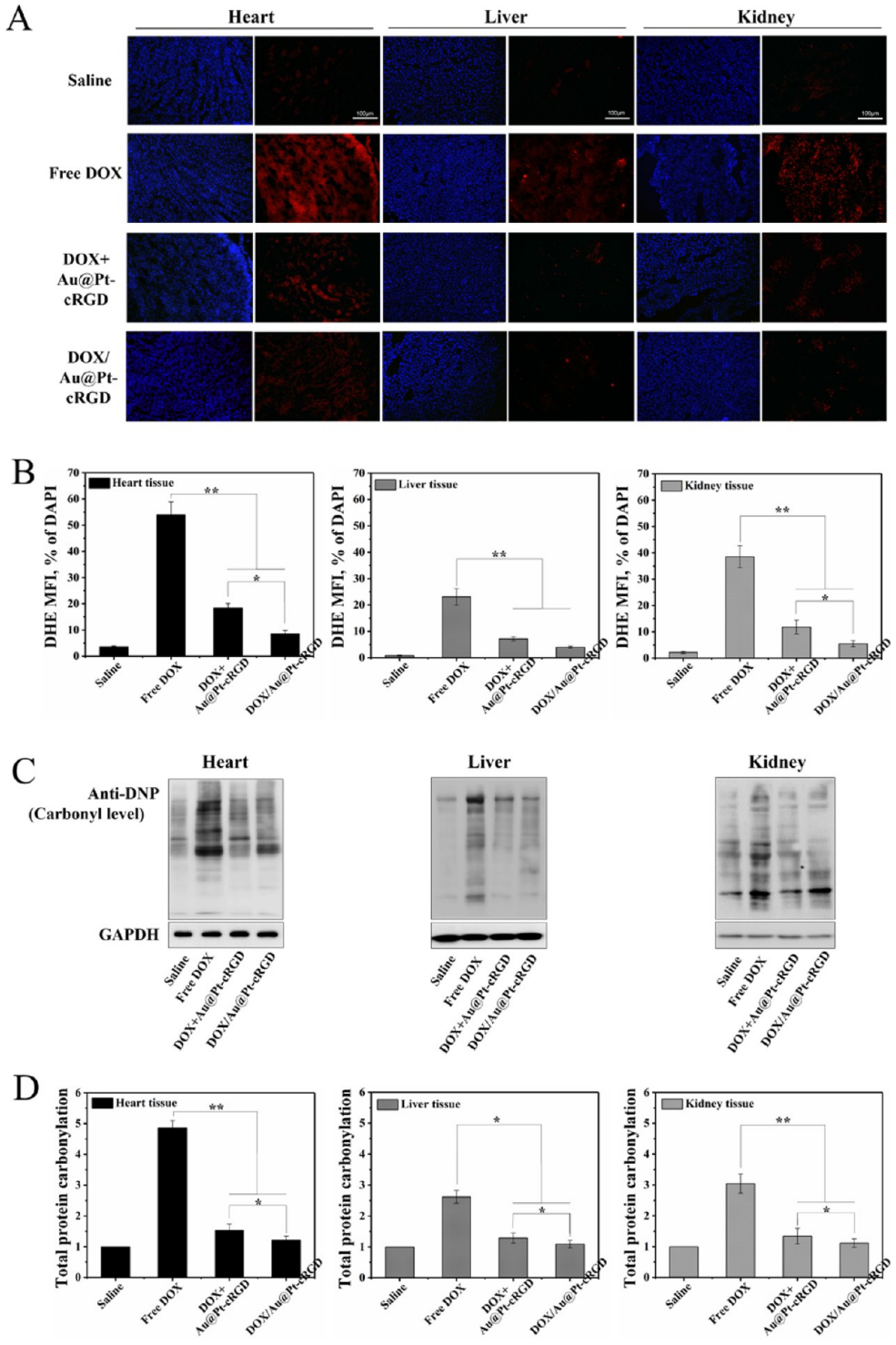

Figure 8. Detection of ROS with DHE Staining: (A) Representative fluorescence microscopy image with different treatments in heart liver and kidney tissue (scale bar = 100 μm). (B) Quantification of DHE staining in heart liver and kidney tissue. (C) Representative immunoblots of protein carboxylation in heart, liver, and kidney tissue lysates. (D) Quantification of total protein carboxylation normalized to total protein in different tissue. Error bars were based on standard deviations (SD) of three mice per group (* $P < 0.05$, ** $P < 0.01$).

carbonylated proteins compared with the subsequent Au@Pt administration followed by DOX treatment (Figure 8C and D). The results demonstrated that the DOX/Au@Pt-cRGD not only can be used as theranostic agent for PAI and PTT/chemotherapy, but also can be used as ROS scavenger for antioxidative stress during chemotherapy.

CONCLUSION

In summary, in order to construct a drug delivery nanocarrier with desired drug delivery properties that could alleviate the side effects of the chemotherapeutics by the nanocarrier itself, Au@Pt nanoparticles with optimized particle size and unique nanoporous structure were successfully synthesized in our study. By physically absorbing with DOX and chemically

DOI: 10.1021/acsami.7b14705
ACS Appl. Mater. Interfaces 2018, 10, 150−164

conjugating with PEG-cRGD, DOX/Au@Pt-cRGD maintained satisfactory stability and enhanced drug loading efficiency. It was noted that this gold-based bimetallic nanoscale platform exhibited stronger NIR absorbance and higher photoconversion efficiency for photoacoustic image-guided enhanced photothermal therapy of MDA-MB-231 tumors. Compared with the control, DOX/Au@Pt-cRGD possessed high tumor accumulation and significantly enhanced photoacoustic signals for *in vivo* imaging. More importantly, PTT and chemotherapy by DOX/Au@Pt-cRGD demonstrated excellent MDA-MB-231 tumor inhibition effect with low laser radiation (1.5 W/cm^2 for 5 min) and low drug dose. Furthermore, this metal-based nanocarrier also alleviated the DOX-introduced cardiomyopathy, hepatic injury, and nephrotoxicity by scavenging ROS. Overall, our results highlight the DOX/Au@Pt-cRGD system with photoacoustic imaging and combined therapeutic features, that exerted unique antioxidative effect upon oxidative stress injury, which could be an ideal candidate in achieving maximal chemo-thermal therapeutic outcomes, suppressing their adverse effects.

MATERIALS AND METHODS

Materials. Gold(III) chloride trihydrate ($HAuCl_4 \cdot 3H_2O$), Pluronic F-127 (F-127), silver nitrate (AgNO3), ascorbic acid, potassium tetrachloroplatinate(II) (K_2PtCl_4), methyl thiazolyl tetrazolium (MTT), Calcein AM, and PI were purchased from Sigma-Aldrich. Thiol poly(ethylene glycol) Succinimidyl Glutaramide (HS-PEG-SGA, MW 3500) was purchased from Jenkem Technology, Inc. Doxorubicin (DOX, MW: 580) was purchased from Dalian Meilun Biotechnology, Co., Ltd. The Oxyblot Protein Oxidation Detection kit was from Millipore, Dulbecco's Modified Eagle Medium (DMEM), antibiotic/antimycotic solution, and fetal bovine serum were purchased from Gibco (Thermo Fisher Scientific, USA). All other solvents and reagents used in this study were certified analytical reagent grade.

Cell Lines. MDA-MB-231 (breast cancer) cell line used in this study was purchased from American Type Culture Collection (ATCC, Rockville, MD), which were grown in DMEM medium supplemented with 10% of FBS, 1% of penicillin/streptomycin, respectively. The cell cultures were maintained in a 37 °C incubator with humidified 5% of CO_2 atmosphere.

Animals. All the animals (Balb/c nude mice, 4−6 weeks old) were all purchased from Beijing HFK Bioscience Co. Ltd., China and kept under SPF condition with free access to standard food and water, and the operation procedures were following the guidelines on animal care and use of State Key Laboratory of Biotherapy, Sichuan University, China.

Preparation of Au@Pt and Its Conjugates. *Synthesis of Au@Pt Nanoparticles.* In a typical synthesis of Au@Pt nanoparticles following a reported protocol[46] (Pt/Au molar ratio = 1.0), 2.0 mL of H_2PtCl_4 solution (25 mM) and 2.0 mL of $HAuCl_4$ solution (25 mM) were mixed with Pluronic F127 (50 mg) in a small flask. After that, 2.0 mL of AA solution (0.25 M) was added, and the mixture was then sonicated at room temperature for 15 min. Then the mixture was aged for another 24 h. The products were purified by centrifuge at 12500 rpm for 10 min, and washed at least three times with 50% ethanol. Finally, the products were dispersed in DI water for further application.

Synthesis of DOX/Au@Pt-cRGD, DOX/Au@Pt-PEG, Au@Pt-DOX. Two mL of Doxorubicin hydrochloride water solution (0.2 mg/mL) was adjusted the pH of 8 by NaOH. Then, 3.6 mg of Au@Pt nanoparticles redispersed in 2 mL of DI water was added. This mixture was sonicated for 5 min and then incubated at room temperature with stirring in the dark for 12 h. After the reaction, cRGD (5 mg) and NHS-PEG-SH (10 mg) were added to the DOX absorbed Au@Pt suspension simultaneously and the reaction was maintained for another 12 h. Subsequently, the incubation product (DOX/Au@Pt-cRGD) was purified by centrifugation at 7500 rpm for 15 min to remove the unconjugated PEG and cRGD in the supernatant. The collected precipitates were redispersed in 2.0 mL DI water for further applications.

DOX/Au@Pt-PEG and Au@Pt-PEG were prepared by similar procedure with DOX/Au@Pt-cRGD, except RGD and/or DOX/RGD were not added in the reaction, respectively.

Characterization. *Morphology and Size Distribution.* The compositions (the contents of Au and Pt) of Au@Pt nanoparticles (Au@Pt-40, Au@Pt-60, Au@Pt-100) were measured by Inductively Coupled Plasma-Atomic Emission Spectrometer (ICP-MS, VG PQ ExCell, TJA). The morphological and structural information on Au@Pt (Au@Pt-40, Au@Pt-60, Au@Pt-100) and its conjugates (Au@Pt-DOX, DOX/Au@Pt-cRGD) were measured by a field-emission high-resolution transmission electron microscope (HRTEM, Tecnai G2 F20 S-TWIN, FEI, American). A dilute solution droplet of the sample was added into 400-mesh carbon-coated copper grid and the excessive solvent was immediately evaporated before microscopy. Energy Dispersive X-ray Spectroscopy (EDX) and line scan were used to semiquantitatively measure the Au and Pt contents and their distribution on the nanoparticles.

The hydrodynamic particle sizes and zeta potentials of Au@Pt, DOX/Au@Pt, DOX/Au@Pt-PEG, and DOX/Au@Pt-cRGD were determined using a Zetasizer Nano-ZS from Malvern Instruments (Zetasizer nano ZS, Malvern, British) at 25 °C, respectively. Polydispersity index was utilized to evaluate the distribution of the nanoparticle population.

Molecular Binding Energy. The binding energy of the Au and Pt in Au or Au@Pt nanoparticles structure was measured by X-ray photoelectron spectroscopy (XPS, XSAM 800, Kratos, UK).

Surface Pore Volume and Pore Size Distribution. The pore volume and pore size distribution of Au@Pt (Au@Pt-40, Au@Pt-60, Au@Pt-100) and its conjugates (Au@Pt-DOX, DOX/Au@Pt-cRGD) were measured by nitrogen adsorption−desorption measurements. Nitrogen adsorption−desorption measurements were performed on an ASAP2020 (Micromeritics, USA) accelerated surface area analyzer at 77 K. Before measuring, all the samples were degassed in a vacuum at 120 °C for at least 6 h.

Optical Properties of Au@Pt and its Conjugates. The absorption spectra of Au@Pt (Au@Pt-40, Au@Pt-60, Au@Pt-100) and its conjugates (Au@Pt-DOX, DOX/Au@Pt-cRGD) were acquired with UV−vis spectrophotometer (Shimadzu, UV-2600).

Photothermal Effect of DOX/Au@Pt-cRGD. The photothermal conversion efficacy of DOX/Au@Pt-cRGD was evaluated. DOX/Au@Pt-cRGD dispersion with different concentrations (0, 12, 25, 50, 100 μg/mL) was irradiated by an 808 nm laser for 5 min light irradiation time. The beam diameter was 2 cm^2 and the power density of laser source was fixed at 1.5 W/cm^2. At definite time intervals, temperature of the dispersion was recorded by portable electronic thermometer with a probe.

To evaluate the stability of the photothermal conversion of DOX/Au@Pt-cRGD, an ON/OFF cycle irradiation experiment was processed. The DOX/Au@Pt-cRGD solution (50 μg/mL of Au@Pt) was irradiated by 808 nm laser for 5 min, and then the laser was turned off. When the temperature of the sample solution recovered to the initial temperature, the laser was turned on again. This process was repeated for eight cycles, and the temperature variation was recorded. At the beginning and end of irradiation cycles, the variation of the UV−vis spectra of DOX/Au@Pt-cRGD was measured by a UV−vis spectrometer, and the morphology of the nanocarriers before or after irradiation was also observed by TEM.

Drug Loading and Releasing Behavior. To calculate the DOX loading efficiency, the supernatants purified by centrifugation-wash for DOX/Au@Pt and DOX/Au@Pt-cRGD suspension were collected, and the unconjugated DOX in the supernatants were further analyzed by UV−vis spectrometer and the absorbance measured at 488 nm.

The DOX loading capacity was calculated according to the formula

DOI: 10.1021/acsami.7b14705
ACS Appl. Mater. Interfaces 2018, 10, 150−164

$$\text{Drug loading(DL)} = (\text{mass of drug absorbed with Au@Pt/total mass of drug and Au@Pt}) \times 100\%$$

Drug release experiments were performed at physiological temperature. DOX/Au@Pt-cRGD (5 mg) were redispersed in 2 mL PBS (10 mM, pH = 7.4), then placed in a dialysis bag with molecular weight cutoff of 8000−14000 and sealed. The releasing medium consisted of 8 mL PBS with different pH (5.0, 6.0, and 7.4, separately). At definite time intervals, the releasing medium was collected and was replaced by fresh buffer at each time point. In the groups treated with NIR laser irradiation, before the releasing mediums were collected, NIR laser (1.5 W/cm^2, 808 nm) was introduced and maintained for 5 min. Then the release medium was collected, and another 8 mL of fresh buffer was added as release medium. All the collected samples were centrifuged (12500 rpm, 10 min) and drug concentration in the supernatants were analyzed and determined by UV−vis spectrometer (absorbance at 488 nm).

Cell Survival of DOX/Au@Pt-cRGD Mediated PTT/Chemotherapy. To investigate the cellular uptake of DOX/Au@Pt-cRGD, the MDA-MB-231 cells were plated on a six-well plate and cultured for 24 h. Next, DOX/Au@Pt-PEG and DOX/Au@Pt-cRGD (25 μg/mL of Au@Pt) were added to each well for incubation in culture medium. At predetermined times, the culture media in the 6-well plates were piped out and the cells were washed by PBS two times. Then, a certain number of cells was collected and washed with PBS three times. The Au and Pt contents were measured by ICP-MS.

To investigate the photothermal ablation and chemotherapy on the survival of the cancer cells, the MDA-MB-231 cell line was used to evaluate the therapeutic coeffect of DOX/Au@Pt-cRGD *in vitro*. The MDA-MB-231cells were seeded at 5 × 10^3 cells per well in a 96-well plate, and incubated with varying concentrations of free DOX, Au@Pt-cRGD, DOX/Au@Pt-PEG, and DOX/Au@Pt-cRGD. After incubation for 4 h, the culture media were all replaced with fresh culture medium, and the cells were cultured for another 24 h. To the groups treated with NIR laser (808 nm, 1.5 W/cm^2), after the addition of fresh culture medium, NIR laser was introduced and the cells were irradiated for 5 min before another 24 h culturing. Frequently, the cell survival was determined by performing MTT assay. The data reported represent the means of triplicate measurements.

In order to visualize the PTT/chemotherapy of cancer cells *in vitro*, live/dead costaining was performed. MDA-MB-231 cells were plated on a six-well plate and preincubated for 24 h. Then, the cells were cocultured with Au@Pt-cRGD, DOX/Au@Pt-PEG, and DOX/Au@Pt-cRGD (25 μg/mL of Au@Pt), respectively. Four hours later, the culture medium of each sample was replaced with fresh DMEM culture medium with penicillin−streptomycin after rinsing once with PBS buffer. Then, the 808 nm laser was introduced. The power of the laser was 1.5 W/cm^2, and the irradiation time was 5 min. The calcein AM/PI costaining was performed immediately after irradiation. The fluorescent images of the cancer cells were obtained by fluorescence microscope (Olympus, Japan).

Enrichment of DOX/Au@Pt-cRGD in Tumor Site *In Vivo*. *In Vitro and In Vivo PA Imaging.* *In vitro* phantom and *in vivo* PA imaging investigations were carried out by the Multi-Spectral Optoacoustic Tomography imaging system (MSOT, MSOT inVision 128, iThera medical GmbH, Germany). MDA-MB-231 tumor model was established on balb/c-nu mice 14 days before PAI *in vivo*. The laser frequency was 10 Hz with average pulse duration of about 10 ns from 680 to 850 nm. The step length was 0.3 mm, and the speed of sound was −36. The transducer array has a central frequency of 10 MHz, which is used to provide a transverse spatial resolution of 75 μm. The temperature of the sink was 34 °C. Model-linear and linear regression were chosen as the reconstruction method and the MSP method, respectively. The spectra of the samples were used as MSP spectra. The MSP background wavelength was 680 nm.

Phantom (prepared using agar and intralipid with diameter of 2 cm) was used to measure the PA signal intensity of the sample *in vitro*.

Biodistribution of the DOX/Au@Pt-cRGD. In order to investigate the biodistribution of the DOX/Au@Pt-PEG and DOX/Au@Pt-cRGD in living mice, the major organs (heart, liver, spleen, lung, kidney, and tumor) of the MDA-MB-231 tumor-bearing mice were excised at 4 and 48 h post-injection, and the Au and Pt contents in these organ tissues were detected by ICP-MS.

Photothermal Conversion In Vivo. MDA-MB-231 tumor-bearing nude mice were used to evaluate the photothermal performance of DOX/Au@Pt-cRGD *in vivo*. After the intravenous administration of saline, DOX/Au@Pt-PEG and DOX/Au@Pt-cRGD, respectively, 8 h later, the mice were anesthetized and then irradiated by an 808 nm laser with a power of 1.5 W/cm^2 for 5 min. The temperature variation of the tumor site was recorded by an infrared imaging device (Fluke, T32).

Therapeutic Efficacy Evaluation of DOX/Au@Pt-cRGD *In Vivo*. MDA-MB-231 tumor model was established in nude mice. After the mean volume of the tumors reached approximately to 100 mm^3, the tumor-bearing mice were randomly divided into 5 groups (n = 5) and intravenously administered with 200 μL of saline, free DOX (1.5 mg/kg, for 4 times), Au@Pt-cRGD + Laser, DOX/Au@Pt-cRGD, and DOX/Au@Pt-cRGD + Laser (DOX dosage was 6 mg/kg per mice, DLC was 4.8%), respectively. Laser irradiation was introduced in Au@Pt-cRGD + Laser and DOX/Au@Pt-cRGD + Laser groups after 8 h injection, and the laser power was settled at 1.5 W/cm^2, with an irradiation time of 5 min. Tumor volumes and body weights were measured every other day with a caliper. The tumor volume was calculated as length × (width)^2 × 1/2. Relative tumor volumes were calculated as V/V_0 (V_0 = tumor volume at the first treatment).

Tumor Tissue Histopathological and Proliferation Study. On the 24th day after the first treatment, the organs and the tumors were harvested, fixed in 10% neutral buffered formalin, processed routinely into paraffin, sectioned, and used for immunohistochemical/immunofluorescence study which was detected by K_i-67 staining and TUNEL staining, respectively.

Alleviation the DOX-Induced Organ Tissue Injury by Au@Pt. Wild-type (WT) C57BL/6 mice were randomly divided to 4 groups: the mice in the control group were given equal volume of saline, one group was treated with one intraperitoneal injection of 200 μL of free DOX (20 mg/kg), one group was treated with two intravenous injections of Au@Pt-cRGD at 1 h and 24 h after administration with free DOX (20 mg/kg), respectively, and the final group was administered DOX/Au@Pt-cRGD (DOX dosage was 10 mg/kg per mice, DLC was 4.8%) intravenously daily for 2 days. On the 10th day after DOX administration, the mice were euthanized. Blood was collected from all sacrificed animals, and the serum obtained by centrifuging the whole blood at 5000 rpm for 15 min. Heart, liver, and kidney tissues were also excised. Parts of samples were fixed for 24 h in 10% neutral buffered formalin for histopathology study, and other organ tissues were frozen and stored at −80 °C until the further ROS detection.

Blood Biochemical Analysis. The biochemical parameters of alanine aminotransferase (ALT), aspartate aminotransferase (AST), blood urea nitrogen (BUN), and creatinine (CRE) were measured by auto biochemistry analyzer (Roche cobas integra 400 plus, Roche, Switzerland).

Histological Analysis. The formalin-fixed tissues were embedded in paraffin, sectioned at 5 mm thickness. The sliced tissues were stained with Hematoxylin and Eosin (H&E), and observed by microscopy (Zeiss OBSERVER D1/AX10 cam HRC).

Detection of ROS in Heart, Liver, and Kidney Tissue. To analyze ROS levels of the DOX-induced oxidative injury model, we used the ROS-responsive dye dihydroethidium (DHE) for tissue staining.[44] DHE is a blue color dye that easily permeates into cells and converts to red fluorescence in the presence of superoxide. Heart, liver, and kidney tissues were sectioned (6 mm) and fixed, and then, the samples were treated with 5 mM of DHE and incubated for 30 min at 37 °C in the dark. After washing, the sections were incubated with 4,6-diamidino-2-phenylindole (DAPI) for 1 min. Images were

DOI: 10.1021/acsami.7b14705
ACS Appl. Mater. Interfaces 2018, 10, 150−164

acquired by fluorescence microscope (Zeiss OBSERVER D1/AX10 cam HRC). Quantification was performed on each section.

Protein carbonylation, as a common biomarker for oxidatively modified proteins, were detected by immunoblotting in heart, liver, and kidney tissues.[47] Protein carbonyls was derivatized to 2,4-dinitrophenyl (DNP) hydrazine and then probed with anti-DNP primary antibody using the Oxyblot Detection kit (Millipore). Quantitation of protein carbonylation was performed by analysis band intensity. The DNP levels of derivatized proteins were normalized by GAPDH and data were expressed as fold change relative to saline treated group.

Statistic Analysis. A statistical analysis was performed using SPSS 15.0 software (IBM corporation, Armonk, NY). The results of multiple group comparisons were all indicated as mean ± standard derivations and analyzed using one-way analysis of variance (ANOVA). $p < 0.05$ was considered statistically significant.

■ ASSOCIATED CONTENT

Supporting Information

The Supporting Information is available free of charge on the ACS Publications website at DOI: 10.1021/acsami.7b14705.

Structural characterization, optical properties, *in vitro* cellular uptake and photoacoustic imaging information, immunohistochemical analysis, blood biochemical analysis, and histological analysis (PDF)

■ AUTHOR INFORMATION

Corresponding Author

*E-mail: anderson-qian@163.com.

ORCID

Zhiyong Qian: 0000-0003-2992-6424

Author Contributions

The manuscript was written through contributions of all authors. All authors have given approval to the final version of the manuscript.

Funding

This work was financially supported by the National Natural Science Fund for Distinguished Young Scholar (NSFC31525009). The National Natural Science Funds (NSFC31600811, 31771096, and NSFC31500809). The Application Fundamental Research Foundation of Sichuan Province Science and Technology Department, China (Grant No. 2016JY0157). Scientific Research Foundation of the Education Department of Sichuan Province, China (Grant No. 15ZA0256). Scientific Research Foundation of the Health and Family Planning Commission of Sichuan Province, China (Grant No. 17PJ556).

Notes

The authors declare no competing financial interest.

■ ACKNOWLEDGMENTS

We thank Dr. Shanling Wang from Analytical & Testing center, Sichuan University, P. R. China for the TEM observation and analysis of the data.

■ REFERENCES

(1) Tacar, O.; Sriamornsak, P.; Dass, C. R. Doxorubicin: an Update on Anticancer Molecular Action, Toxicity and Novel Drug Delivery Systems. *J. Pharm. Pharmacol.* **2013**, *65* (2), 157−170.

(2) Carvalho, F. S.; Burgeiro, A.; Garcia, R.; Moreno, A. J.; Carvalho, R. A.; Oliveira, P. J. Doxorubicin-induced Cardiotoxicity: from Bioenergetic Failure and Cell Death to Cardiomyopathy. *Med. Res. Rev.* **2014**, *34* (1), 106−135.

(3) Lv, L.; Qiu, K.; Yu, X.; Chen, C.; Qin, F.; Shi, Y.; Ou, J.; Zhang, T.; Zhu, H.; Wu, J. Amphiphilic Copolymeric Micelles for Doxorubicin and Curcumin Co-delivery to Reverse Multidrug Resistance in Breast Cancer. *J. Biomed. Nanotechnol.* **2016**, *12* (5), 973−985.

(4) Osman, A.-M. M.; Al-Harthi, S. E.; AlArabi, O. M.; Elshal, M. F.; Ramadan, W. S.; Alaama, M. N.; Al-Kreathy, H. M.; Damanhouri, Z. A.; Osman, O. H. Chemosensetizing and Cardioprotective Effects of Resveratrol in Doxorubicin-treated Animals. *Cancer Cell Int.* **2013**, *13* (1), 52.

(5) Rocha, V. C. J.; de Aragão França, L. S.; de Araújo, C. F.; Ng, A. M.; de Andrade, C. M.; Andrade, A. C.; de Souza Santos, E.; da Cruz Borges-Silva, M.; Macambira, S. G.; Noronha-Dutra, A. A. Protective Effects of Mito-TEMPO Against Doxorubicin Cardiotoxicity in Mice. *Cancer Chemother. Pharmacol.* **2016**, *77* (3), 659−662.

(6) Octavia, Y.; Tocchetti, C. G.; Gabrielson, K. L.; Janssens, S.; Crijns, H. J.; Moens, A. L. Doxorubicin-induced Cardiomyopathy: from Molecular Mechanisms to Therapeutic Strategies. *J. Mol. Cell. Cardiol.* **2012**, *52* (6), 1213−1225.

(7) Li, Q.; Liang, J.; You, X.; Liu, X.; Wu, H.; Gao, W.; Wen, Y.; Wu, J.; Xu, X.; Zhang, F. A Novel Reactive Oxygen Species Triggered Polymeric Nanoplatform for Controlled Drug Delivery and Cancer Therapy. *J. Biomed. Nanotechnol.* **2017**, *13* (5), 513−521.

(8) Glasgow, M. D.; Chougule, M. B. Recent Developments in Active Tumor Targeted Multifunctional Nanoparticles for Combination Chemotherapy in Cancer Treatment and Imaging. *J. Biomed. Nanotechnol.* **2015**, *11* (11), 1859−1898.

(9) Srinivasarao, M.; Galliford, C. V.; Low, P. S. Principles in the Design of Ligand-targeted Cancer Therapeutics and Imaging Agents. *Nat. Rev. Drug Discovery* **2015**, *14* (3), 203−219.

(10) Sapsford, K. E.; Algar, W. R.; Berti, L.; Gemmill, K. B.; Casey, B. J.; Oh, E.; Stewart, M. H.; Medintz, I. L. Functionalizing Nanoparticles with Biological Molecules: Developing Chemistries that Facilitate Nanotechnology. *Chem. Rev.* **2013**, *113* (3), 1904−2074.

(11) Yu, L.; Chen, Y.; Chen, H. H_2O_2-responsive Theranostic Nanomedicine. *Chin. Chem. Lett.* **2017**, *28* (9), 1841−1850.

(12) Yoshitomi, T.; Ozaki, Y.; Thangavel, S.; Nagasaki, Y. Redox Nanoparticle Therapeutics to Cancer-increase in Therapeutic Effect of Doxorubicin, Suppressing its Adverse Effect. *J. Controlled Release* **2013**, *172* (1), 137−143.

(13) Song, Y.; Lou, B.; Cheng, J.; Zhao, P.; Lin, C.; Wen, X. Redox-responsive Amphipathic Dextran Nanomicelles for Solid Tumor Therapy. *J. Biomed. Nanotechnol.* **2016**, *12* (12), 2083−2096.

(14) Pedone, D.; Moglianetti, M.; De Luca, E.; Bardi, G.; Pompa, P. P. Platinum Nanoparticles in Nanobiomedicine. *Chem. Soc. Rev.* **2017**, *46* (16), 4951−4975.

(15) Jawaid, P.; Rehman, M. U.; Zhao, Q. L.; Takeda, K.; Ishikawa, K.; Hori, M.; Shimizu, T.; Kondo, T. Helium-based Cold Atmospheric Plasma-induced Reactive Oxygen Species-mediated Apoptotic Pathway Attenuated by Platinum Nanoparticles. *J. Cell. Mol. Med.* **2016**, *20* (9), 1737−1748.

(16) Li, J.; Guan, M.; Wang, T.; Zhen, M.; Zhao, F.; Shu, C.; Wang, C. Gd@ C82-(ethylenediamine) 8 Nanoparticle: A New High-efficiency Water-soluble ROS Scavenger. *ACS Appl. Mater. Interfaces* **2016**, *8* (39), 25770−25776.

(17) Asharani, P.; Lianwu, Y.; Gong, Z.; Valiyaveettil, S. Comparison of the Toxicity of Silver, Gold and Platinum Nanoparticles in Developing Zebrafish Embryos. *Nanotoxicology* **2011**, *5* (1), 43−54.

(18) Zhang, N.; Zhu, D.; Li, F.; Hua, H.; Tian, X.; Zhao, Y. Low Density Lipoprotein Peptide-Conjugated Gold Nanorods for Combating Gastric Cancer. *J. Biomed. Nanotechnol.* **2017**, *13* (2), 134−143.

(19) Mulgaonkar, A.; Moeendarbari, S.; Silvers, W.; Hassan, G.; Sun, X.; Hao, Y.; Mao, W. Hollow Gold Nanoparticles as Efficient In Vivo Radiosensitizing Agents for Radiation Therapy of Breast Cancer. *J. Biomed. Nanotechnol.* **2017**, *13* (5), 566−574.

(20) Khan, S. A.; Kanchanapally, R.; Fan, Z.; Beqa, L.; Singh, A. K.; Senapati, D.; Ray, P. C. A Gold Nanocage−CNT Hybrid for Targeted

Imaging and Photothermal Destruction of Cancer Cells. *Chem. Commun.* **2012**, *48* (53), 6711−6713.
(21) Liu, Y.; Ashton, J. R.; Moding, E. J.; Yuan, H.; Register, J. K.; Fales, A. M.; Choi, J.; Whitley, M. J.; Zhao, X.; Qi, Y. A Plasmonic Gold Nanostar Theranostic Probe for *in vivo* Tumor Imaging and Photothermal Therapy. *Theranostics* **2015**, *5* (9), 946−960.
(22) Ataee-Esfahani, H.; Wang, L.; Nemoto, Y.; Yamauchi, Y. Synthesis of Bimetallic Au@ Pt Nanoparticles with Au Core and Nanostructured Pt Shell toward Highly Active Electrocatalysts. *Chem. Mater.* **2010**, *22* (23), 6310−6318.
(23) Tang, F.; Li, L.; Chen, D. Mesoporous Silica Nanoparticles: Synthesis, Biocompatibility and Drug Delivery. *Adv. Mater.* **2012**, *24* (12), 1504−1534.
(24) Lee, D.-E.; Koo, H.; Sun, I.-C.; Ryu, J. H.; Kim, K.; Kwon, I. C. Multifunctional Nanoparticles for Multimodal Imaging and Theragnosis. *Chem. Soc. Rev.* **2012**, *41* (7), 2656−2672.
(25) Horcajada, P.; Chalati, T.; Serre, C.; Gillet, B.; Sebrie, C.; Baati, T.; Eubank, J. F.; Heurtaux, D.; Clayette, P.; Kreuz, C. Porous Metal-Organic-Framework Nanoscale Carriers as a Potential Platform for Drug Delivery and Imaging. *Nat. Mater.* **2010**, *9* (2), 172−178.
(26) Zhao, R.; Han, X.; Li, Y.; Wang, H.; Ji, T.; Zhao, Y.; Nie, G. Photothermal Effect Enhanced Cascade-Targeting Strategy for Improved Pancreatic Cancer Therapy by Gold Nanoshell@ Mesoporous Silica Nanorod. *ACS Nano* **2017**, *11* (8), 8103−8113.
(27) He, W.; Liu, Y.; Yuan, J.; Yin, J.-J.; Wu, X.; Hu, X.; Zhang, K.; Liu, J.; Chen, C.; Ji, Y. Au@ Pt Nanostructures as Oxidase and Peroxidase Mimetics for Use in Immunoassays. *Biomaterials* **2011**, *32* (4), 1139−1147.
(28) Tongsakul, D.; Nishimura, S.; Ebitani, K. Platinum/Gold Alloy Aanoparticles-supported Hydrotalcite Catalyst for Selective Aerobic Oxidation of Polyols in Base-free Aqueous Solution at Room Temperature. *ACS Catal.* **2013**, *3* (10), 2199−2207.
(29) Song, H. M.; Anjum, D. H.; Sougrat, R.; Hedhili, M. N.; Khashab, N. M. Hollow Au@ Pd and Au@ Pt Core−Shell Nanoparticles as Electrocatalysts for Ethanol Oxidation Reactions. *J. Mater. Chem.* **2012**, *22* (48), 25003−25010.
(30) Li, Y.; Ding, W.; Li, M.; Xia, H.; Wang, D.; Tao, X. Synthesis of Core−Shell Au−Pt Nanodendrites with High Catalytic Performance via Overgrowth of Platinum on *in situ* Gold Nanoparticles. *J. Mater. Chem. A* **2015**, *3* (1), 368−376.
(31) Liu, X.; Zhang, X.; Zhu, M.; Lin, G.; Liu, J.; Zhou, Z.; Tian, X.; Pan, Y. PEGylated Au@ Pt Nanodendrites as Novel Theranostic Agents for Computed Tomography Imaging and Photothermal/Radiation Synergistic Therapy. *ACS Appl. Mater. Interfaces* **2017**, *9* (1), 279−285.
(32) Peng, J.; Dong, M.; Ran, B.; Li, W.; Hao, Y.; Yang, Q.; Tan, L.; Shi, K.; Qian, Z. One-for-All"-Type, Biodegradable Prussian Blue/Manganese Dioxide Hybrid Nanocrystal for Trimodal Imaging-guided Photothermal Therapy and Oxygen Regulation of Breast Cancer. *ACS Appl. Mater. Interfaces* **2017**, *9* (16), 13875−13886.
(33) Peng, J.; Qi, T.; Liao, J.; Chu, B.; Yang, Q.; Qu, Y.; Li, W.; Li, H.; Luo, F.; Qian, Z. Mesoporous Magnetic Gold "Nanoclusters" as Theranostic Carrier for Chemo-photothermal co-Therapy of Breast Cancer. *Theranostics* **2014**, *4* (7), 678−692.
(34) Liao, J.; Li, W.; Peng, J.; Yang, Q.; Li, H.; Wei, Y.; Zhang, X.; Qian, Z. Combined Cancer Photothermal-chemotherapy based on Doxorubicin/Gold Nanorod-loaded Polymersomes. *Theranostics* **2015**, *5* (4), 345−356.
(35) Liao, J.; Wei, X.; Ran, B.; Peng, J.; Qu, Y.; Qian, Z. Polymer Hybrid Magnetic Nanocapsules Encapsulating IR820 and PTX for External Magnetic Field-guided Tumor Targeting and Multifunctional Theranostics. *Nanoscale* **2017**, *9* (7), 2479−2491.
(36) Huang, L.; Han, Y.; Dong, S. Highly-Branched Mesoporous Au−Pd−Pt Trimetallic Nanoflowers Blooming on Reduced Graphene Oxide as an Oxygen Reduction Electrocatalyst. *Chem. Commun.* **2016**, *52* (56), 8659−8662.
(37) Minati, L.; Antonini, V.; Dalla Serra, M.; Speranza, G. Multifunctional Branched Gold−Carbon Nanotube Hybrid for Cell Imaging and Drug Delivery. *Langmuir* **2012**, *28* (45), 15900−15906.
(38) Manson, J.; Kumar, D.; Meenan, B. J.; Dixon, D. Polyethylene Glycol Functionalized Gold Nanoparticles: the Influence of Capping Density on Stability in Various Media. *Gold Bull.* **2011**, *44* (2), 99−105.
(39) Roti Roti, J. L. Cellular Responses to Hyperthermia (40−46 °C): Cell Killing and Molecular Events. *Int. J. Hyperthermia* **2008**, *24* (1), 3−15.
(40) Yao, C.; Tian, J.; Wang, H.; Zhang, D.-W.; Liu, Y.; Zhang, F.; Li, Z.-T. Loading-free Supramolecular Organic Framework Drug Delivery Systems (sof-DDSs) for Doxorubicin: Normal Plasm and Multidrug Resistant Cancer Cell-adaptive Delivery and Release. *Chin. Chem. Lett.* **2017**, *28* (4), 893−899.
(41) Aryal, B.; Jeong, J.; Rao, V. A. Doxorubicin-induced Carbonylation and Degradation of Cardiac Myosin Binding Protein C Promote Cardiotoxicity. *Proc. Natl. Acad. Sci. U. S. A.* **2014**, *111* (5), 2011−2016.
(42) Aioub, M.; Panikkanvalappil, S. R.; El-Sayed, M. A. Platinum-Coated Gold Nanorods: Efficient Reactive Oxygen Scavengers That Prevent Oxidative Damage toward Healthy, Untreated Cells during Plasmonic Photothermal Therapy. *ACS Nano* **2017**, *11* (1), 579−586.
(43) Sack, M.; Alili, L.; Karaman, E.; Das, S.; Gupta, A.; Seal, S.; Brenneisen, P. Combination of Conventional Chemotherapeutics with Redox-active Cerium Oxide Nanoparticles-A Novel Aspect in Cancer Therapy. *Mol. Cancer Ther.* **2014**, *13* (7), 1740−1749.
(44) Park, S.; Yoon, J.; Bae, S.; Park, M.; Kang, C.; Ke, Q.; Lee, D.; Kang, P. M. Therapeutic Use of H_2O_2-responsive Anti-oxidant Polymer Nanoparticles for Doxorubicin-induced Cardiomyopathy. *Biomaterials* **2014**, *35* (22), 5944−5953.
(45) Szwed, M.; Kania, K. D.; Jozwiak, Z. Molecular Damage Caused by Generation of Reactive Oxygen Species in the Redox Cycle of Doxorubicin-transferrin Conjugate in Human Leukemia Cell Lines. *Leuk. Lymphoma* **2015**, *56* (5), 1475−1483.
(46) Marques-Aleixo, I.; Santos-Alves, E.; Mariani, D.; Rizo-Roca, D.; Padrão, A. I.; Rocha-Rodrigues, S.; Viscor, G.; Torrella, J. R.; Ferreira, R.; Oliveira, P. J. Physical Exercise Prior and During Treatment Reduces Sub-chronic Doxorubicin-induced Mitochondrial Toxicity and Oxidative Stress. *Mitochondrion* **2015**, *20*, 22−33.
(47) Yan, L. J. Analysis of Oxidative Modification of Proteins. *Cur. Protoc. Protein. Sci.* **2009**, *4*, 14.4.1−14.4.28.

DOI: 10.1021/acsami.7b14705
ACS Appl. Mater. Interfaces 2018, 10, 150−164